AFRL-AFOSR-JP-TR-2016-0060

Understanding combustion and soot formation in diesel engines

Shawn Kook
Office of Naval Research
875 N. Randolph
Arlington, VA 22203

09/09/2016
Final Report

Air Force Research Laboratory
Air Force Office of Scientific Research

Asian Office of Aerospace Research and Development
Unit 45002, APO AP 96338-5002

REPORT DOCUMENTATION PAGE

Form Approved
OMB No. 0704-0188

1. REPORT DATE *(DD-MM-YYYY)*	2. REPORT TYPE	3. DATES COVERED *(From - To)*
09-09-2016	Final	01 Mar 2014 to 29 Feb 2016

4. TITLE AND SUBTITLE
Understanding combustion and soot formation in diesel engines

5a. CONTRACT NUMBER

5b. GRANT NUMBER
FA2386-14-1-4049

5c. PROGRAM ELEMENT NUMBER
61102F

6. AUTHOR(S)
Shawn Kook

5d. PROJECT NUMBER

5e. TASK NUMBER

5f. WORK UNIT NUMBER

7. PERFORMING ORGANIZATION NAME(S) AND ADDRESS(ES)
Office of Naval Research
875 N. Randolph
Arlington, VA 22203 US

8. PERFORMING ORGANIZATION REPORT NUMBER
N/A

9. SPONSORING/MONITORING AGENCY NAME(S) AND ADDRESS(ES)
AOARD
UNIT 45002
APO AP 96338-5002

10. SPONSOR/MONITOR'S ACRONYM(S)
AFRL/AFOSR IOA

11. SPONSOR/MONITOR'S REPORT NUMBER(S)
AFRL-AFOSR-JP-TR-2016-0060

12. DISTRIBUTION/AVAILABILITY STATEMENT
Distribution Code A: Approved for public release, distribution is unlimited.

13. SUPPLEMENTARY NOTES

14. ABSTRACT

This project investigated biodiesel combustion and soot processes using four complementary approaches including computational modelling based on high performance computers, laser diagnostic experiments in an optically accessible diesel engine, direct in-flame soot particle sampling and structure analysis, and engine performance and emissions testing.

15. SUBJECT TERMS
AOARD, Combustion

16. SECURITY CLASSIFICATION OF:			17. LIMITATION OF ABSTRACT	18. NUMBER OF PAGES	19a. NAME OF RESPONSIBLE PERSON
a. REPORT	b. ABSTRACT	c. THIS PAGE			ROBERTSON, SCOTT
Unclassified	Unclassified	Unclassified	SAR	29	19b. TELEPHONE NUMBER *(Include area code)* +81-42-511-7008

Standard Form 298 (Rev. 8/98)
Prescribed by ANSI Std. Z39.18

FINAL REPORT

Project title: Understanding combustion and soot formation in biodiesel fuelled diesel engines

Lead Institute and Principal Investigator (Technical Point of Contact):
Shawn Kook
Associate Professor and Director of Research
School of Mechanical and Manufacturing Engineering
The University of New South Wales
Address: Mechanical Engineering Building (J17), UNSW Sydney, NSW 2052, Australia
Tel: +61 2 9385 4091 Fax: +61 2 9663 1222 Email: s.kook@unsw.edu.au

Administrative Point of Contact:
Daniel Owens
Director, Grants Management Office
Address: Level 3, Rupert Myers Building South Wing (M15), UNSW Kensington Campus, NSW 2052, Australia
Tel: +61 2 9385 7230 Email: mygrants.gmo@unsw.edu.au

NCAGE Code: 0PDL5
DUNS Number: 751020900
Grant Total from ONR/ONRG:
$175,000 (1st year: $75,000 and 2nd year: $100,000)

Period of Performance: 10 Jun 2014 – 9 Jun 2016

From: Andrew Higier, Ph.D.
Associate Director
U.S. Office of Naval Research Global (ONR Global)
Phone: +65 6476-9360
Fax: +65 6476-9084
Email: andrew.m.higier.civ@mail.mil

Dr. Cung Vu
Associate Director
U.S. Office of Naval Research Global (ONR Global)
Tel: +65 6476 9360
Email: cung.vu.civ@mail.mil

Participating US Institution and PI:
Name: LTC David Hopper
Affiliation: Asian Office of Aerospace Research and Development (AOARD)
Address: 7-23-17 Roppongi, Minato-ku, Tokyo, Japan 106-0032
Tel: +81-42-511-2002 E-mail: david.hopper@us.af.mil

1. Summary

This project investigated biodiesel combustion and soot processes using four complementary approaches including computational modelling based on high performance computers, laser diagnostic experiments in an optically accessible diesel engine, direct in-flame soot particle sampling and structure analysis, and engine performance and emissions testing. The work is motivated by the need to clarify biodiesel combustion, harmful effects of soot on health and the environment, and implications of soot for infrared signatures of ships. Empirically it is known that biodiesel usually results in reduced soot emissions but the mechanisms behind this were virtually unexplored. Also, how this reduction is correlated to the flame development of biodiesel was not fully understood. This project has bridged these gaps by successfully developing a transported probability density function (TPDF) model for numerical simulations of soot. Moreover, we performed laser-based imaging diagnostics for detailed understanding of soot formation/oxidation processes, which led to major findings such that not only the soot is less for biodiesel but also soot formation is delayed; and biodiesel soot is surrounded by hydroxyl radicals resulting in enhanced oxidation. From the in-flame soot particles sampling, biodiesel soot structural details are discovered such as smaller particle size, more fragile structures, and more reactive nanostructures, all of which suggest easier soot oxidation for biodiesel. Finally, engine performance tests show significantly reduced engine-out smoke/NOx emissions as expected; however, to maintain diesel power output, biodiesel should be blended in diesel at up to 40%. These new findings provide a clear motivation to further investigate the influence of key biodiesel molecular structure parameters such as carbon chain length and the degree of unsaturation of carbon double bonds, as summarized in the concluding remarks section.

2. Background

According to the U.S. Navy's Energy Goals, a half of total energy consumption should come from renewable sources, including biofuels, by 2020. One of the action items is to deploy a "Great Green Fleet", a carrier strike group fuelled by alternative sources of energy by 2016. For instance, during the 2012 Rim of the Pacific exercise involving 22 nations, warships running on a 50-50 mix of diesel and biodiesel were successfully demonstrated.

In contrast to conventional biodiesel fuels from food-crop-based feedstocks, next generation biodiesel fuels can be produced in large amounts from dedicated energy crops and micro-algae [1-3]. These feedstocks are domestic resources and therefore help protect national security by reducing the dependence on the volatile global oil market. It is important to understand however that there is no single biofuel production solution that can provide sufficient fuel to cover all of the needs. In addition, fossil fuels will increasingly come from alternative feedstocks, leading to greatly increased diversity in the fuel supply.

This diversification presents an opportunity and challenge for the control of diesel combustion. The use of biodiesel, in particular, has been studied in commercial diesel engines in pure and blended formulations, with the majority of these studies reporting a reduction of soot, carbon monoxide (CO), and unburned hydrocarbon (uHC), while emissions of oxides of nitrogen (NO_x) and fuel consumption increase [4-5]. These emissions trends are the result of complex interactions between physical and chemical processes occurring inside the engine cylinder. Biodiesel has significantly different physical properties compared to regular diesel fuel, including a higher boiling-point temperature, viscosity, and density. In addition, it has a significantly different chemical structure -

notably, biodiesel is an oxygenated fuel, affecting air-fuel mixing stoichiometry as well as chemical kinetics and pollutant formation.

Even between different biodiesel fuels there are significant variations in molecular structure which impact performance and emissions, for example depending on the type of algae, fuels having from 10 to 20 atoms in the carbon chain can be produced, with varying degrees of saturation [6]. Folding in the increased diversity of fossil fuels as well as other biofuel options such as furanic fuels, it is clear that it will be critical to the Navy to have the ability to match new-generation feedstocks, new production process, new fuels, and compatible engine technology that will lead to the most practical and sustainable alternatives to petroleum. A crucial element of this will be the clear understanding of combustion that can lead to the prediction of engine performance and emissions when a wide variety of alternative fuels are used.

Among pollutant emissions, soot is arguably the most important to the US Navy. Soot particles are very small and can therefore penetrate deep into the respiratory system. They have a very high surface area that is structured at the molecular level, which enables them to bind with other toxins and to interact with organic molecules. These features can lead to a number of health issues [7]. In the short term, exposure can present problems of immediate operational concern such as dizziness, headache, and shortness of breath, while in the long term there are serious cardiopulmonary risks. Soot as a solid particle is also an extremely efficient radiator which if present in an exhaust plume contributes significantly to a ship or other vehicle's infrared signature. It absorbs radiation strongly even at low concentrations, which is thought to contribute to climate change [8]. Finally, soot in large amounts is visible to the eye, potentially contributing to the public's perceptions of the environmental cleanliness of Navy ships and vehicles.

Therefore, the need to predict and reduce soot exhaust emissions from the Navy's diesel engines is clear. As earlier explained, these emissions are fuel dependent. Past studies investigated the effect of biodiesel on in-cylinder soot concentrations (e.g. [**Error! Reference source not found.**]) and reported a consistent reduction of soot emissions when biodiesel is injected instead of conventional diesel; however, little was understood about the mechanism of this reduction.

References

1. Energy technology perspectives – scenarios & strategies to 2050, International Energy Agency, OECD Publications, 2006.
2. World Energy Outlook 2009. International Energy Agency. OECD Publications, 2009.
3. Official Journal of the European Union, Directive 2009/28/EC of the European Parliament and of the Council of 23 April 2009. Official Journal L140, 16-62, 2009.
4. Monyem, A., Van Gerpen, J.H., The effect of biodiesel oxidation on engine performance and emissions, Biomass & Bioenergy, Vol. 20, pp. 317-325, 2001.
5. Lapuerta, M., Armas, O., Rodríguez-Fernández, J., Effect of biodiesel fuel on diesel engine emissions, Progress in Energy and Combustion Science, Vol. 34, pp. 198-223, 2008.
6. Hu, Q., Sommerfeld, M., Jarvis, E., Ghirardi, M., Posewitz, M., Seibert, M., Darzins, A., (2008), The Plant J., Vol. 54(4), pp. 621-639.
7. Wittmaak, K., In search of the most relevant parameter for quantifying lung inflammatory response to nanoparticle exposure: particle number, surface area, or what?, Environmental Health Perspectives, Vol. 115(2), pp. 187-194, 2007.
8. Ramanathan, V., Carmichael, G., Global and regional climate changes due to black carbon, Natural Geoscience, Vol. 1(4), pp. 221-227, 2008.
9. Mueller, C.J., Boehman, A.L., Martin, G.C., An experimental investigation of the origin of increased NO_x emissions when fueling a heavy-duty compression-ignition engine with soy biodiesel, SAE Paper 2009-01-1792, SAE Int. J. Fuels Lubr., 2009.

3. Project Objectives

This project aims to uncover the mechanisms of soot reduction in biodiesel-fueled engines by:

1) Developing and validating a detailed modeling approach which can predict soot formation/oxidation in diesel engine-like high-pressure and high-temperature ambient gas conditions and its impact on radiation heat transfer;
2) Performing high-speed visualisation of visible flames and laser-based imaging diagnostics in an optically-accessible diesel engine to obtain in-cylinder distributions of high-temperature reaction zones and soot within the biodiesel flame;
3) Conducting innovative in-flame soot particles sampling in a working diesel engine to provide size and structure information of soot aggregates and primaries; and
4) Evaluating the engine performance and emissions of biodiesel fuels blended in regular diesel to find practical operating conditions.

The outcome is a more complete understanding of the mechanisms behind biodiesel combustion and soot, and greater confidence for the ability to predict fuel effects on combustion and soot emissions in general.

4. Approach

Numerical Simulation

A detailed numerical simulation approach has been developed and applied to model soot formation and oxidation for a surrogate fuel (n-dodecane), as shown in Figure 1. This modelling approach improves our ability in predicting soot production and provides a greater level of insight into the soot mechanisms and how these depend on the fuel's oxygen moieties. Following recent work in the group, the approach was based on the composition transported probability density function (TPDF) method. This approach solves for the joint statistics of the chemical species concentrations and temperature, which has the distinct advantage compared with other methods in that the chemical reaction rates appear in closed form. The approach employed a 54 species *n*-dodecane chemical mechanism and an acetylene-based two-equation soot model coupled with a time-dependent Reynolds-averaged k−ε turbulence model and a Lagrangian discrete phase model for the liquid spray.

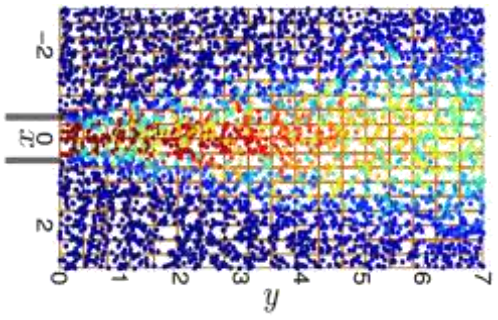

Figure 1. Transported probability density function (TPDF) modelling approach

Optical/Laser-based Imaging Diagnostics

Two laser-based imaging diagnostics have been performed in an optically-accessible diesel engine (Figure 2) for regular diesel and a selected biodiesel surrogate fuel. Methyl decanoate was used for this purpose as it is an oxygenated fuel with a long stretched carbon chain structure of fatty acid methyl esters (i.e. biodiesel). Its cetane number of 52 is similar to regular diesel (51) and the fuel molecular structure is similar to n-dodecane used for the development of soot modelling. A high pulse-energy (>100 mJ) Nd:YAG laser at 1064 nm was used to induce soot incandescence signal, *i.e.* planar laser-induced incandescence (PLII). Two-dimensional distributions of PLII signals help understand the soot distributions within diesel/biodiesel flames. In addition, planar laser-induced

fluorescence of hydroxyl (OH) radicals was performed to visualise spatial and temporal evolution of high-temperature reaction zones, i.e. OH-PLIF. By putting together the PLII and OH-PLIF signals, not only the soot formation but also the soot oxidation process was analyzed. Three additional line-of-sight integrated imaging of cool-flame chemiluminescence, excited OH (OH*) chemiluminescence, and hot soot luminosity were also performed to provide complementary information to planar laser images.

In-flame soot sampling and structure analysis

At the same operating conditions of laser-based imaging diagnostics, soot particles were sampled by exposing transmission electron microscope (TEM) grids directly to diesel/biodiesel flames inside the cylinder of the engine. Soot particles were sampled via thermophoresis between hot soot particles within the flame and the cool TEM grid stored in the sampling probe that was fixed on the cylinder

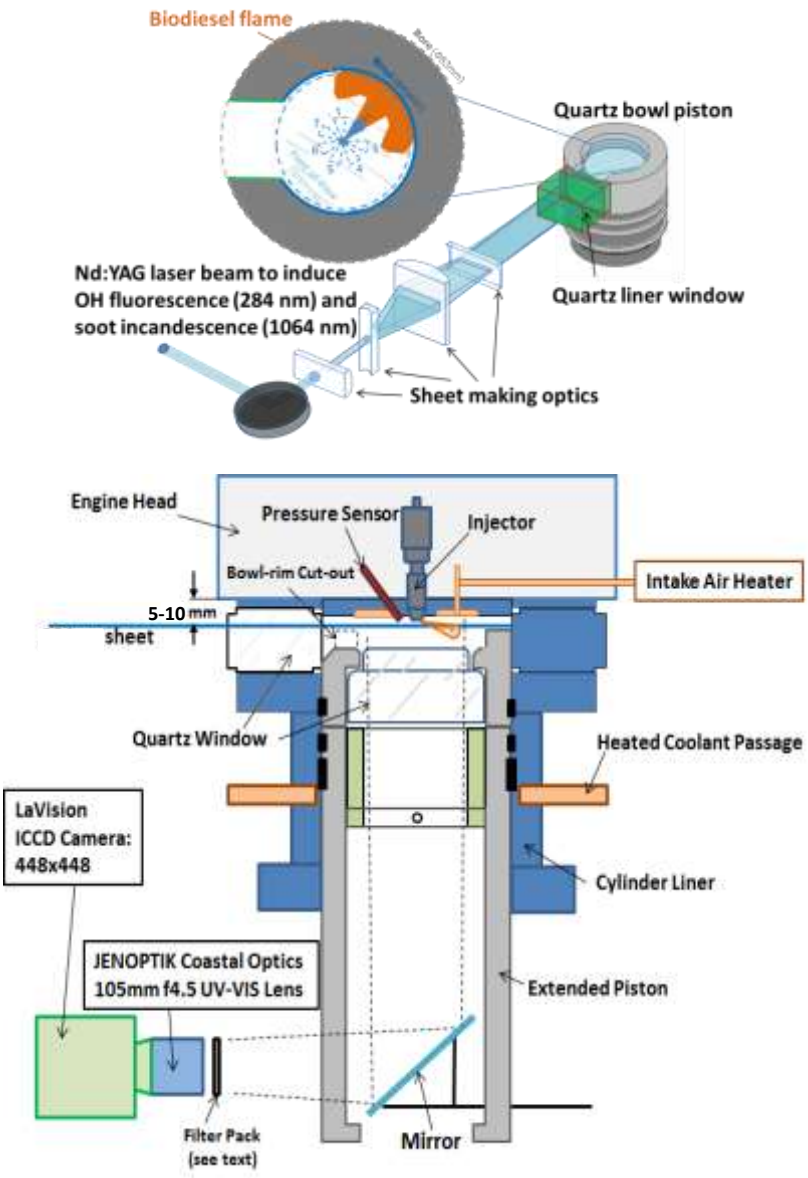

Figure 2. Optical diesel engine used for laser-based imaging diagnostics and soot particles sampling.

liner. Two different types of 3-mm diameter TEM grids were used to collect soot particles for the morphology analysis and nanoscale internal structure analysis using 400-mesh, carbon-coated copper grids (Emgrid CF400-Cu) and 300-mesh, 150-μm-thick lacy grids (Emgrid LC300-Cu), respectively. The grids were held at a fixed location in the bowl-rim cut-out region (see Figure 2) while they were exposed to sooting flames. The collected soot samples were imaged using two TEMs: one with the accelerating voltage of 120 kV and the point resolution 0.38 nm (JEOL 1400) and the other with the accelerating voltage of 200 kV and the point resolution 0.25 nm (Philips CM200). The digitised images were then post-processed to obtain key morphology parameters such as primary particle diameter, aggregate radius of gyration and fractal dimension as well as nanostructure parameters such as carbon fringe length, tortuosity and fringe-to-fringe separation.

Engine performance tests

Fundamental research performed using surrogate fuels was supported by engine performance and emissions testing conducted using biodiesel produced using trans-esterification of triglycerides. Two different production methods were used: one through a chemical catalytic conversion process using NaOH based on methanol moiety and the other through an enzyme catalytic conversion process using a commercial lipase (Novozyme 435) and ethanol. The oxygen concentration in these neat biodiesel is estimated at 14.04% by mass, which means 12.55% and 1.49% less carbon and hydrogen, respectively, compared to regular diesel. The calorific value of these neat biodiesel (39 MJ/kg) was much lower than regular diesel (41.66 MJ/kg); therefore, the neat biodiesel was mixed with regular diesel to produce three different biodiesel blends including B10, B25, and B40 for engine performance and emissions testing. As shown in Figure 3, a single-cylinder "non-optical" diesel engine was used for these tests. The single-cylinder diesel engine shares the production engine head and common-rail fuel injection system of a four-cylinder small-bore engine, widely available in the global market. The engine was operated at fixed speed of 2000 revolutions per minute (RPM) at which the referred production engine generates the maximum torque. A piezo-electric pressure transducer (Kistler 6056A) was used to measure the in-cylinder pressure traces. The pressure data were recorded for 100 cycles for each engine operating condition and then used to obtain an average pressure trace, indicated mean effect pressure (IMEP), and the coefficient of variation of IMEP (CoV of IMEP). The apparent heat release rate (aHRR) was also calculated from the in-cylinder pressure trace. From the aHRR trace, the ignition delay was estimated by reading the time between the start of injection (SOI) and the start of combustion (SOC). The aHRR trace was also used to analyse burn durations for both the initial burn (CA10 to CA50) and late-cycle burn (CA50 to CA90). For each engine operating condition, engine-out emissions were measured. We used an opacimeter (Horiba MEXA-600S, accuracy: ±0.15 m-1 light absorption coefficient) to measure the smoke emissions, a chemiluminescence-type gas analyser (Ecotech 9841AS, 1% accuracy) for NOx emissions, and a non-dispersive infrared (NDIR) analyser (Horiba MEXA-584L, 1.7% accuracy) for unburnt hydrocarbon (uHC) and carbon monoxide (CO) emissions.

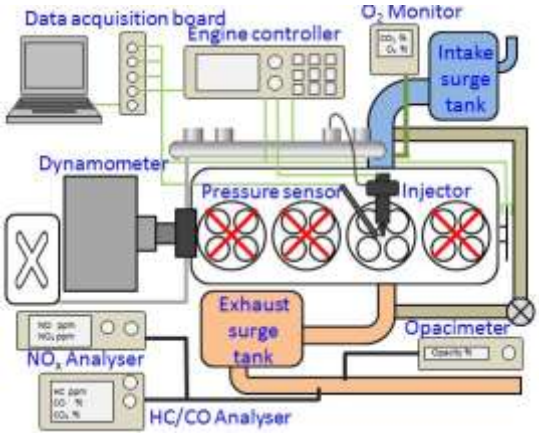

Figure 3. Schematic diagram of single-cylinder diesel engine and diagnostic tools

5. Results and Outcomes

The project has completed successfully according to the schedule of tasks and milestones as summarized in the table below:

Tasks	Months after contract award							
	3	6	9	12	15	18	21	24
Task 1: Numerical simulation of sooting flames								
Subtask 1: The implementation of the soot model into the existing TPDF code			♦					
Subtask 2: Redevelopment of the reduced chemical kinetic mechanism				♦				
Subtask 3: Validation of the resulting model against existing data from a constant volume chamber.					♦			
Subtask 4: Detailed analysis of the modeling.								♦
Task 2: Laser-based imaging of in-cylinder soot distribution								
Subtask 1: Optical engine and fuelling system setup								
Subtask 2: Two-camera high-speed imaging of natural luminosity		●						
Subtask 3: Optics and laser setup								
Subtask 4: OH-PLIF measurement					●			
Subtask 5: Soot-PLII measurement								●
Task 3: Sampled soot particle morphology analysis								
Subtask 1: In-flame soot particles sampling								
Subtask 2: Transmission electron microscope imaging							■	
Subtask 3: Image post-processing								■
Task 4: Engine performance and emissions testing								
Subtask 1: Effect of biodiesel production method				Δ				
Subtask 2: Effect of biodiesel blending ratio							Δ	
Review and report								

Milestones:

♦ – Numerical simulation results and source code

● – Optical diagnostics results and images

■ – Soot structure results and images

Δ – Engine performance results

Milestone 1: Numerical simulation of sooting flames

The soot modelling work has produced five papers (**Publication 1-5**) in which technical details and a complete set of results are found. The work reports the first soot modelling and also the first radiation modelling using the TPDF framework for diesel engine conditions. In this report, only a brief summary of major findings are summarized.

Temporal evolution of a sooting flame

Figure 1-1 portrays the temporal evolution of the spatial distribution of characteristic quantities involved in auto-ignition and soot formation at different time instants: 0.5, 0.7 and 0.9 ms. From left to right: mean temperature, mass fractions of CH_2O, OH and C_2H_2 and soot volume fraction. The black line represents the mean stoichiometric mixture fraction. The first time is selected just after auto-ignition when the flame starts to develop. At this early time, a discrete amount of acetylene is present in concomitance with high temperatures and fuel rich conditions. However, for soot, there is some delay for formation. The CH_2O and OH show the typical complementary distribution where CH_2O is depleted when high-temperature reactions take place. The second time instant coincides with the soot onset time. An important observation is that, along the time instants 0.5, 0.7 and 0.9 ms, the distribution of CH_2O and the flame base location remain practically unchanged. This is consistent with experimental studies reporting a rapid - statistical - stabilization of the flame base after auto-ignition. Figure 1-1 shows that after auto-ignition, changes in the flame structure manifest downstream, where an increase of the fuel rich volume close to the spray tip is observed, leading to an enlargement of the C_2H_2 spatial extent downstream-wise.

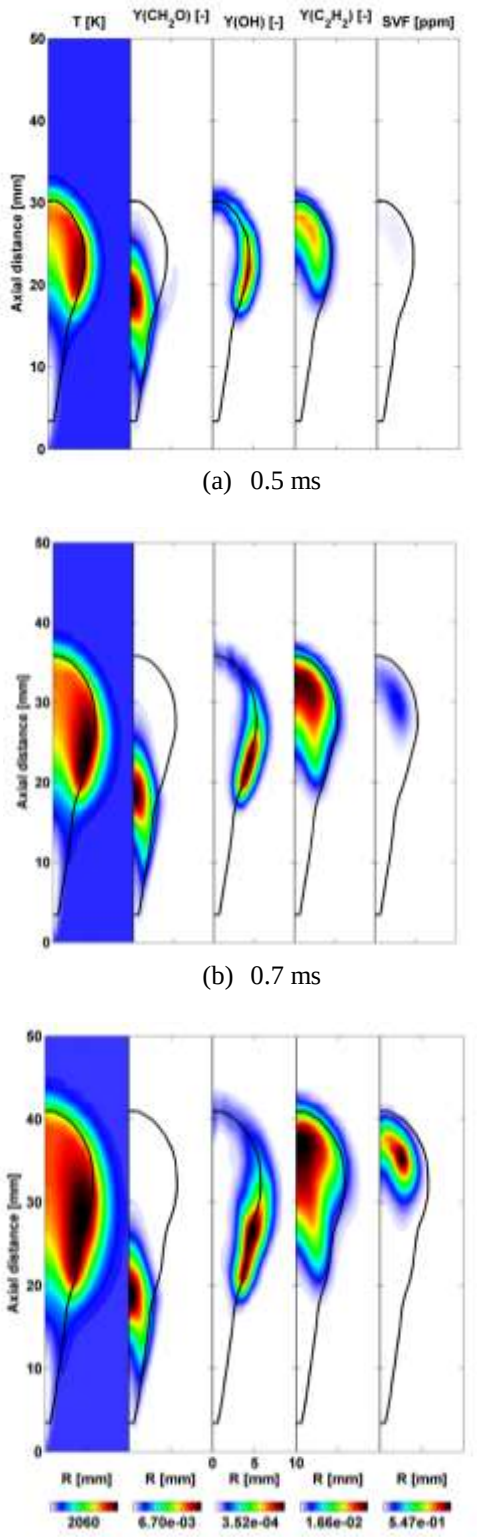

(a) 0.5 ms

(b) 0.7 ms

(c) 0.9 ms

Figure 1-1. Temporal evolution of flame and soot structures at 0.5, 0.7 and 0.9 ms. From left to right: temperature, mass fraction of CH_2O, OH and C_2H_2 and soot volume fraction. The number in the color bar indicates the maximal value.

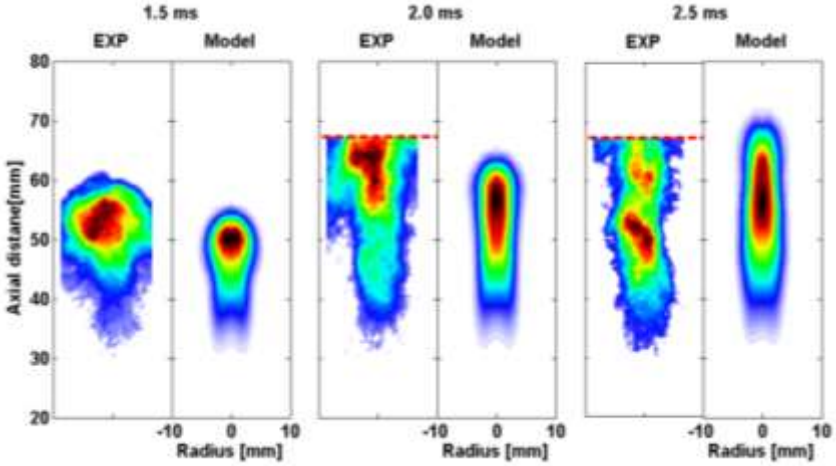

Figure 1-2. The ensemble-averaged KL maps (left side) comparison with numerical TPDF method (right side) at 1.5 ms, 2.0 ms, 2.5 ms. Experimental data from measurements performed in a constant-volume combustion chamber at high-pressure, high-temperature ambient gas conditions relevant to diesel engine conditions.

Soot is first formed close to the tip at an axial distance of around 35 mm from the injector tip. Interestingly, the first soot is formed slightly off-axis due to the high temperatures present there and does not coincide to the current C_2H_2 peak concentration. The modelled spatial contours of the soot volume fraction are compared with the available ensemble-averaged images of the experimental optical thickness (KL) at different time instants as shown in Figure 1-2 for 1.5, 2 and 2.5 ms. The diffused back illumination measurement technique employed in the experimental results is a line-of-sight method which enables to quantify the two-dimensional line-of-sight soot optical thickness. Only during the quasi-steady period, enough samples are present to perform a tomographic reconstruction of the optical thickness and, therefore, a quantitative soot volume fraction can be extracted as will be shown in Figure 1-3. During the first 3 ms only a qualitative comparison can be performed and should provide information only concerning the soot region in the form of normalized quantities. Red dashed lines have been drawn to facilitate the reader. It is clearly shown that the TPDF model is able to reproduce the region of high soot concentration at different time instants.

The iso-contours of different quantities related to the flame structure at 2 (upper) and 4 ms (lower) are illustrated in Figure 1-3. From left to right, mixture fraction, temperature, computed mass fractions of O_2, OH and CH_2O are presented. The black line represents the stoichiometric mixture fraction as a marker for the high temperature region and discriminates the mean fuel rich from the mean fuel lean region. The spray flame tip propagates with time. The temperature contours show the overall location of the flame. The oxygen is not completely consumed at the stoichiometric iso-line and a certain amount of oxygen is present

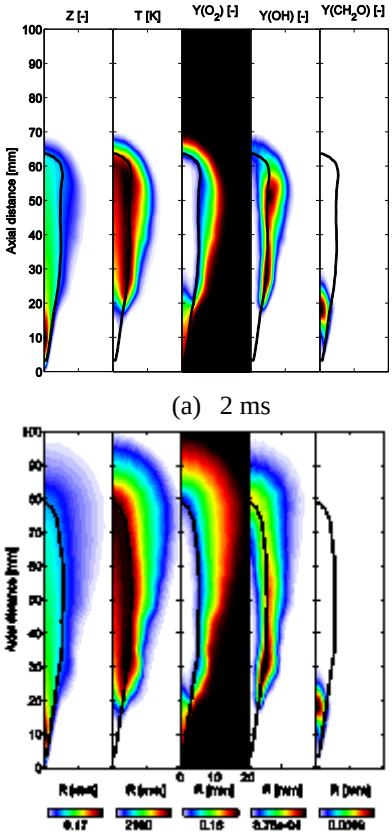

(a) 2 ms

(b) 4 ms

Figure 1-3: Spatial distribution of relevant quantities for flame characterization at 2 (upper) and 4 ms (lower). From left to right: mean mixture fraction, temperature, mass fractions of oxygen, OH and CH_2O.

in the mean fuel rich region. This is a typical feature for models accounting for turbulence-chemistry interaction (TCI). As expected, the location of peak OH mass fraction is aligned with the stoichiometric line, while the cool flame structure (marked by CH_2O) is present closer to the injector and does not vary as described in Figure 1-1. Due to the strong axial gradient of mean temperature and OH mass fraction, the flame base is clearly visible.

Figure 1-4 shows the temporal evolution of other soot-related quantities at 2 (upper) and 4 ms (lower), from left to right: mass fraction of C_2H_2, soot volume fraction (ppm), surface growth, oxidation by O_2 and OH. The soot precursor (C_2H_2) is present in the fuel rich region downstream of the flame base. High concentrations axially begin at around 25 mm and extend up to 50-60 mm. The peak value is located approximately at 35-40 mm. There is a clear spatial shift between C_2H_2 and soot due to the temporal history of soot formation, which requires C_2H_2 as well as a certain inception time to nucleate and to growth into larger soot particles. Interestingly, the peak C_2H_2 location (35 mm) coincides with the axial soot onset at 4 ms but also to the location of first soot appearance as shown in Figure 1-1 (b and c). The axial extent of the soot surface growth lies between C_2H_2 and soot. This is due to the dependence of the surface growth rate on both, C_2H_2 and the particle surface area. Therefore, high rates of surface growth are obtained where considerable C_2H_2 and soot are simultaneously present.

Soot oxidation by O_2 and OH are displayed with a positive sign, although oxidation has a negative source term as it reduces the soot mass. Oxidation by O_2 is mainly in the outer part of the soot region whereas oxidation by OH is more within the flame and the high soot concentration region. Soot oxidation has a strong dependence O_2 and OH distributions predicted by the model. For the tested conditions of this project, the relative contribution of O_2 and OH to the soot oxidation is comparable with slightly more oxidation by O_2. The relative importance of the oxidation by OH is expected to increase by increasing the ambient oxygen concentration.

In summary, the soot simulation employing the transported probability density function (TPDF) method shows a good agreement in lift-off length and the soot peak location with the experimental values. In particular, the soot volume fraction at quasi-steady conditions is very well reproduced. The location of the peak acetylene concentration approximately coincides with both the quasi-steady axial soot onset as well as the location of the first soot formation. The relative importance of soot formation and oxidation with respect to acetylene, O_2, and OH are clarified. Overall, it was shown that for the TPDF model is a powerful method for the simulation of combustion and soot formation for spray flames.

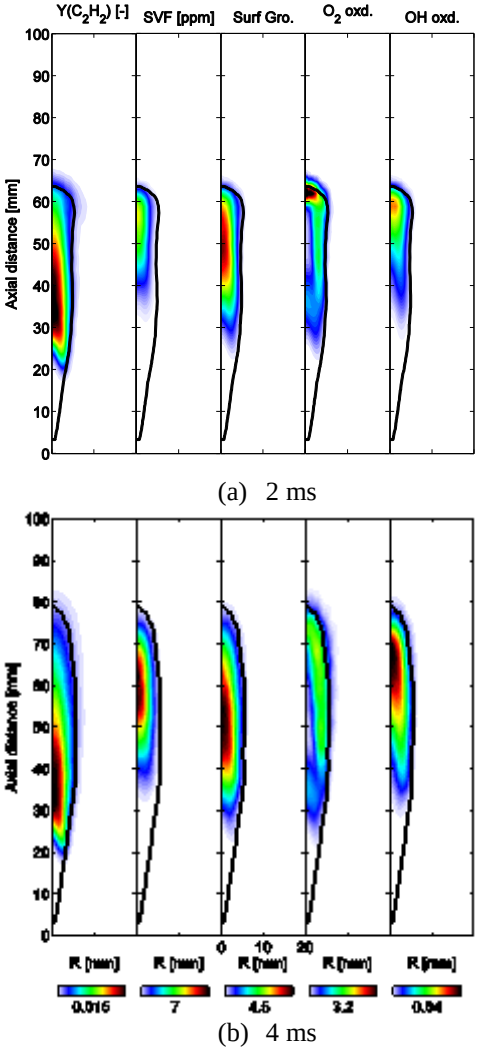

(a) 2 ms

(b) 4 ms

Figure 1-4: Spatial distribution of mass fraction of acetylene (C_2H_2), soot volume fraction and chemistry related soot sources in [1/s] (surface growth, oxidation by O_2 and OH) at 2 (upper) and 4ms (lower). Numbers in the colorbar indicate maximal values.

Soot radiation heat transfer

Upon the successful development and implementation of soot modelling, the importance of radiative heat transfer on the combustion and soot formation characteristics has been studied. Radiation from both gas-phase and soot particles has been included and assumed as gray. Three different solvers for the radiative transfer equation have been employed: the discrete ordinate method, the spherical-harmonics method and the optically thin assumption. The radiation models have been coupled with the transported probability density function method for turbulent reactive flows and soot, where unresolved turbulent fluctuations in temperature and composition are included and therefore capturing turbulence-chemistry-soot-radiation interactions.

Figure 1-5 depicts the spatial distribution of the three most radiative species (soot, CO_2 and H_2O) in conjunction with their respective Planck mean absorption coefficient obtained using the TPDF model at 4 ms after start of injection. Note that these spatial distributions are comparable and only minor differences are observed. The black lines represent the stoichiometric mixture fraction. Numbers drawn at the color bars are the minima and maxima values of the respective quantity. Concerning the radiative species, soot is present in the fuel rich region downstream from the lift-off location (here 16 mm), as expected. The maximal reported value for the soot volume fraction is 7 ppm and the maximal mean absorption coefficient is 35.5 m^{-1}.

In the ambient gas before start of injection there is a considerable amount of CO_2 (mass fraction Y_{CO2}~0.09) and H_2O (Y_{H2O}~0.03), which arise from the premixed pre-burn of a C_2H_2-H_2-O_2-N_2 mixture to enable the generation of the targeted ambient pressure, temperature and oxygen mole fraction at the start of injection. The CO_2 mass fraction peaks along the stoichiometric region. In the fuel region, there is a considerable amount of CO, which has not been converted to CO_2 yet. On the other hand, a high concentration of H_2O mass fraction is homogeneously distributed within the entire fuel-rich cross-section. It is observed that the CO_2 mean absorption coefficient is much higher than the one of H_2O and soot, in particular in the fuel-lean region. This is due to the increase of the absorption coefficient for lower temperatures. The peak magnitude of α_{CO2} is 3.7 times higher and 1.4 times lower for α_{H2O} in comparison with α_{soot}. This means the radiation effects of gas-phase species are more dominant than the soot radiation.

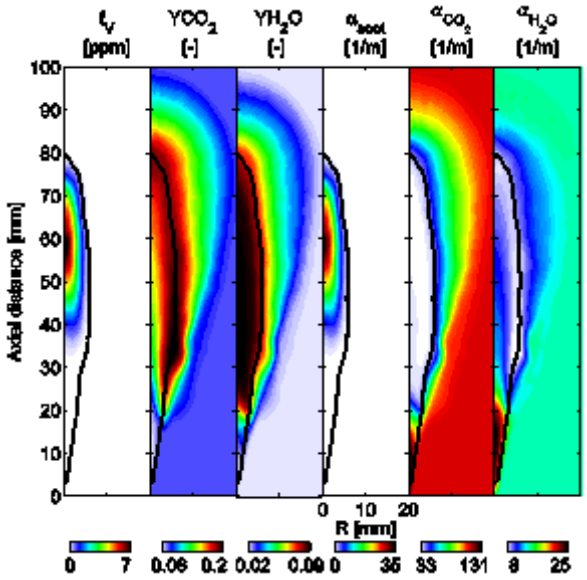

Figure 1-5. Spatial distribution of flame structure quantities using the TPDF model at 4 ms. From left to right: soot volume fraction (ppm), mass fraction of CO_2, H_2O and their respective mean absorption coefficients, respectively.

Figure 1-6 shows spatial distributions of various quantities related to radiation obtained using the discrete ordinate method (DOM) approach in conjunction with two different combustion models: the well-mixed (upper) and the TPDF model (lower). From left to right: temperature, total absorption coefficient (i.e. $\alpha_{soot} + \alpha_{gas\text{-}phase}$), radiative absorption and emission rate, net radiation source term (defined as positive for a heat loss) and rate of temperature change induced by radiation ($T_{rate}=S_{qrad}/(\rho C_p)$).

The temperature contour shows the overall spread of the flame. The major difference between the two combustion models is the thickness of the reaction zone. A comparatively thin layer has been observed for the well-mixed (WM) model in comparison with the TPDF model where the reaction zone is more distributed due to the consideration of turbulent fluctuations within a cell. For the WM approach it results in an increase of the peak temperature by about 150-200K, which can have a considerable influence on the radiation emission.

The total absorption coefficient (second from left) is essentially the sum of the soot, CO_2 and H_2O contributions illustrated in Figure 1-5. The minimal value of around 40 m^{-1} is found along the stoichiometric iso-line in conjunction with the maximal temperature. Higher values are encountered in the oxidizer ambient and the peak value is located in the evaporation region due to the lower temperature. Both combustion models qualitatively exhibit the same characteristics.

Radiation absorption (negative when radiation is absorbed) shows a peak in concomitance with the soot region and moderate values outside the sooty region with increasingly smaller absorption towards the pure ambient composition. The radiation emission rate (positive when radiation is emitted) shows the high values along the stoichiometric iso-line due to the high temperature – although the absorption coefficient is minimal – which is dominating due to the forth power dependence. However, the radiation emission maximal values are in the soot region, where the soot radiation is added to the gas-phase radiation emission.

The net radiation source term (positive when radiation is emitted) is displayed together with the characteristic rate of change of temperature due to radiation (denoted as T_{rate}) expressed in K/ms. The latter provides a feeling for the impact of radiation on the flame temperature. The distribution of these two quantities is practically the same, apart from the local differences in ρC_p. T_{rate} shows its maxima along the stoichiometric line. A gradual decrease of the cooling rate is found in the fuel rich and lean regions. Interestingly, the spray periphery – particularly between 20 and 60 mm from the injector tip – is subjected to a slight increase of the temperature (1-2 K/ms) due to the strong absorption of radiation emitted from the flame.

In summary, results show that the gas-phase (mostly CO_2 and H_2O species) has a higher contribution to the net radiation heat transfer compared to soot. The effect of radiation absorption was found to be important and the typical radiation time scale is observed to overlap with the long injection duration, leading to a moderate influence on the temperature distribution. The flame lift-off length is not affected by radiation and differences in soot formation are perceivable but only minor.

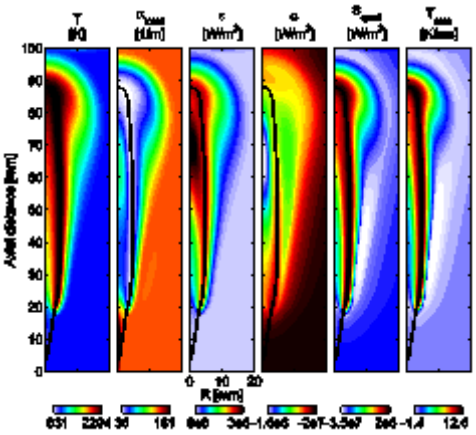

(a) Well-mixed model

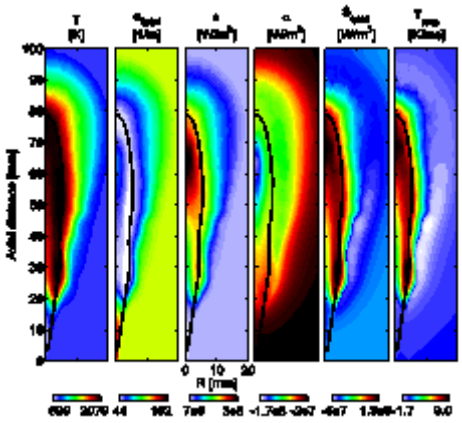

(b) Transported PDF Method

Figure 1-6. Spatial distribution of temperature, total mean absorption coefficient, radiative absorption, emission, source term and temperature rate of change at 4 ms for the WM (upper) and TPDF (lower) models using the DOM method.

Milestone 2: Planar laser-based imaging of hydroxyl and soot

The laser-based imaging diagnostics have been performed using methyl decanoate, a biodiesel surrogate fuel, firstly to understand the overall flame and soot development inside the cylinder of the engine. The same diagnostics were also repeated for regular diesel fuel in the same engine for a direct comparison between a diesel flame and a biodiesel flame in terms of OH and soot. Full data and detailed discussions are found in 4 papers (**Publication 6-9**) that this experimental investigated has produced. Only a brief summary is provided in this report.

Development of a fuel jet, OH, and soot

Figure 2-1 displays the images corresponding to the ignition delay period. Shown in the top row are the fuel-PLIF images taken at 7 mm below the cylinder head for three different crank angles of -6, -4, and -2°CA aTDC. The fuel-PLIF images show that the methyl decanoate jet penetrates freely upon the start of injection before it impinges on the bowl wall at -4°CA aTDC. After the wall-impingement, the fuel jet travels along not only the bowl wall but also along the bottom of the piston bowl as seen at -2°CA aTDC. Shown in the middle row of Fig. 8 are the fuel-PLIF images at the same 7 mm laser plane from TDC to 4°CA aTDC. When these images are combined using yellow for the offline signal and blue for the online OH-PLIF, however, they overlap in most of the jet area and appear in white color. Therefore, the PLIF signals are interpreted as fuel-PLIF. The images show that the fuel jet penetrates further along the bowl wall reaching half of the bowl circumference at 4°CA aTDC. At the same time, the fuel jet appears to bounce off the bowl wall and travels back towards the nozzle. Figure 2-1 shows that the cool-flame signals first appear near the jet axis and in the wall-jet head region at 2°CA aTDC before it grows quickly, matching the size of the fuel jet region in just two crank angles.

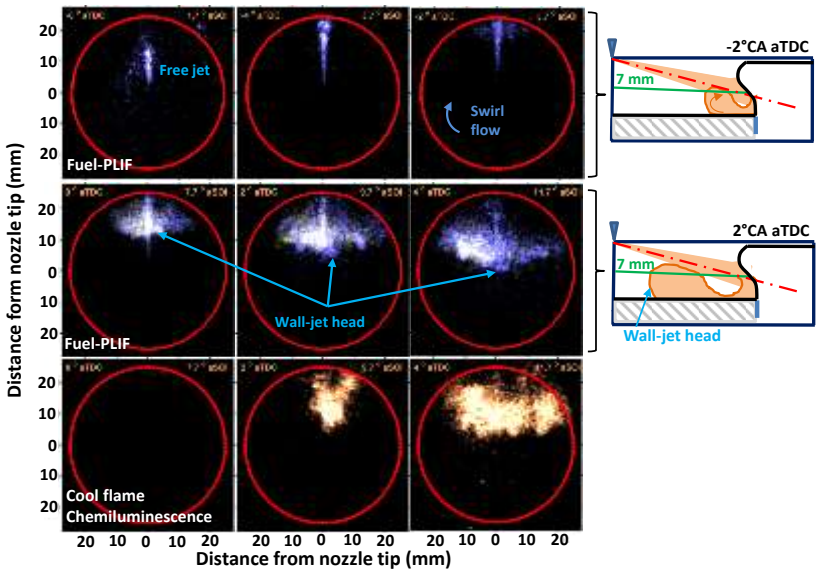

Figure 2-1 Planar laser induced fluorescence (PLIF) signals and cool-flame chemiluminescence signals during the ignition delay period. Also shown on the bottom row are the cool-flame signals corresponding to the images on the middle row.

Figure 2-2 shows the OH* chemiluminescence images that are pseudo-colored with light blue (top row) and the combined online/offline OH-PLIF images at 7 mm below the cylinder head (bottom row) for various crank angles of 5~9°CA aTDC. It is seen that the first OH* signal appears within the cool-flame boundary and on the right to the jet axis, before they grow further in the radial direction. Interestingly, the growth on the right side occurs at a faster rate than that on the left side. This was due to the effect of in-cylinder swirl flow. This led to the delayed second-stage ignition on the up-swirl side. The OH* chemiluminescence signals grow rapidly and by 7°CA aTDC, almost half of the bowl area is filled up with OH* signals and at 9°CA aTDC, OH* is found throughout the

bowl area. The OH* chemiluminescence signals are line-of-sight integrated and thus the information they carry is limited. Therefore, the combined online/offline OH-PLIF images taken at 7 and 9 mm below the cylinder head are shown in Figure 2-2. The PLIF image at 5°CA aTDC displays that the signals are mostly yellow (as on the far left) or white (as on the left to the jet axis) in both laser planes, suggesting that the fuel fluorescence is still dominant. However, from the 7 mm plane, it is noticeable that the signals on the right to the jet axis are blue dominant with minimal or no yellow, indicating that OH radicals develop in this region as the high-temperature reaction starts to occur. This then explains that the first detected OH* chemiluminescence signal was not from the near nozzle region but from the tip of the penetrating wall-jet. This is consistent with the location of first-stage ignition such that the high-temperature reaction was originated from the head vortex region where the mixing was locally enhanced. At later crank angles, signals from the fuel fluorescence (i.e. yellow and white) diminish quickly and by 9°CA aTDC, mostly OH signals are found. However, the yellow-colored fuel region is still observed near the wall-impingement point at both 7 and 9 mm below the cylinder head. It was noted that the end of injection occurred at 7.5°CA aTDC and thus the fuel fluorescence signals near the wall were likely from the last portion of the fuel injection where the injection rate declines. The low momentum fuel would induce slower penetration and due to the limited air entrainment near the wall-impingement point, the mixtures in this region could be relatively richer.

As the high-temperature reactions continue to occur, the fuel near the bowl wall seen in Fig. 2-2 is consumed quickly. This is clearly noticed in the OH-PLIF images at later crank angles of 10 to 17.5°CA aTDC, as shown in Figure 2-3. In the top row, the online/offline combined OH-PLIF images taken at 7 mm below the cylinder head are presented, in which the signals are purely blue OH-PLIF. Since the injection ended at 7.5°CA aTDC and the aHRR continued to decline at this imaging time, it was identified as the mixing-controlled burn phase. An interesting trend observed

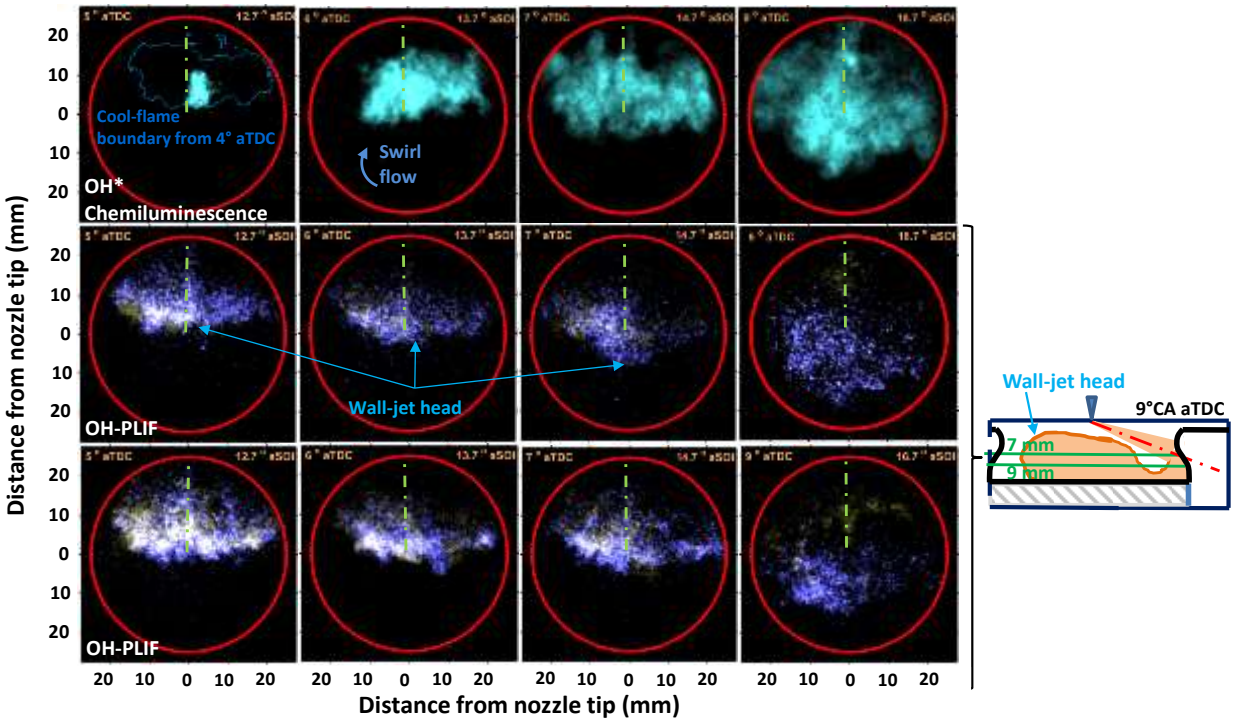

Figure 2-2. OH* chemiluminescence images (top) and corresponding planar laser induced fluorescence (PLIF) signals of OH (online/offline combined) at 7 mm (middle) and 9 mm (bottom) below the cylinder head during the premixed burn phase.

from the OH-PLIF images is that strong OH signals persist for a long while. The downward penetration of reacting wall-jet continued until the OH signals are found near the opposite side of the bowl wall at 10°CA aTDC. Then, the overall flame structure based on OH distributions does not change much until 17.5°CA aTDC. By contrast, marked variations are found in soot distributions as shown in the PLII images taken at the same laser plane and at the same crank angles. The red-colored images of PLII signals are presented in the middle row of Figure 2-3. It was noted that the PLII imaging was performed at earlier crank angles but no signals were observed until the start of mixing-controlled burn at around 10°CA aTDC. It should be considered that methyl decanoate used in the present study is a very low-sooting fuel, which contributed to the delayed soot formation despite no dilution conditions. The PLII images also show an interesting trend such that the soot signals first appear in the wall-impingement point of the jet. As mentioned previously, this is the region with limited mixing and thus locally rich mixtures are expected, explaining the high soot formation. The soot signals near the wall-impingement point continues to grow between 10 and 13°CA aTDC with increasing numbers of soot pockets with various sizes and shapes. An interesting trend observed from the PLII image at 13°CA aTDC is that the signals are stronger and take up larger space on the right side of the jet axis. This should be explained by the swirl flow in the clockwise direction such that relatively richer mixture on the down-swirl side led to higher soot formation than that in the leaner mixture formed on the up-swirl side due to the wall-jet travelling against the swirl flow. It is also noticeable that from 13 to 17.5°CA aTDC, the soot pockets appear to be divided into two groups with each flowing along the bowl wall in either up-swirl or down-swirl direction. At 15°CA aTDC, the soot signals are absent near the wall-impingement point and the soot pockets appear to shrink in size compared to those at 13°CA aTDC, suggesting that the soot oxidation occurs while the pockets flow along the bowl wall. To further discuss the soot oxidation, the OH-PLIF and PLII images are combined and presented in the bottom row of Figure 2-3. The images clearly indicate that the soot pockets are surrounded by OH radicals at 10~13°CA aTDC. However, at 15°CA aTDC, the OH signals start to disappear from the wall-impingement region where the strong soot signals were found at earlier crank angles. This might suggest that the OH radicals were consumed in the oxidation of soot particles, consistent with the modelling results.

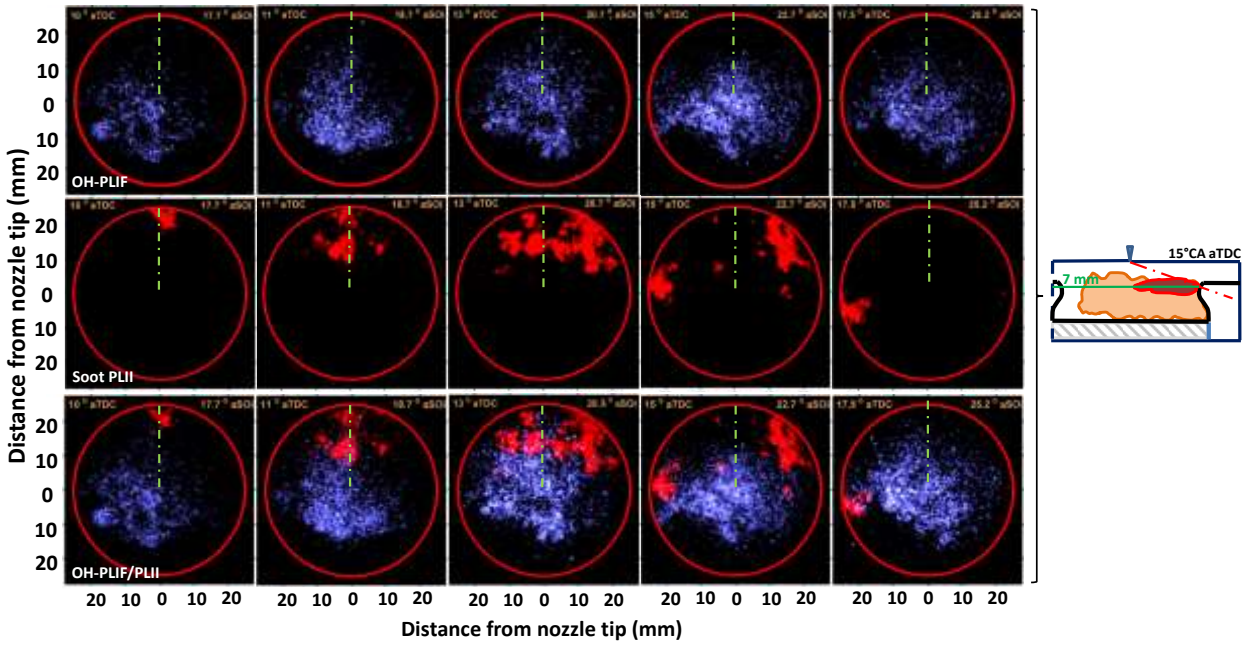

Figure 2-3. Planar laser induced fluorescence (PLIF) signals of OH (online/offline combined, top), planar laser-induced incandescence (PLII, middle) of soot, and the combined image (bottom) during the mixing-controlled burn phase.

Comparison of flame and soot distributions between regular diesel and biodiesel

Figure 2-4 shows the combined OH-PLIF and PLII images obtained during the main combustion event for both regular diesel (left) and methyl decanoate (right). The planar laser images were captured for three different planes of 7, 9, and 11 mm below the cylinder head. The line-of-sight integrated images of OH* chemiluminescence are also presented at the top. The figure shows marked variations of high-temperature reaction zones (i.e. OH) and soot between the two fuels. Firstly, the OH* signals grow much faster for methyl decanoate, which is likely related to fuel molecular structures such as long stretched carbon chain and the presence of O atoms. The disappearance of OH* signals is also faster than that of regular diesel as OH is consumed to oxidize soot more actively. The OH-PLIF/PLII images show a consistent trend such that the soot signals (colored in red) of methyl decanoate diminish at a higher rate. It is obvious that regular diesel had a serious issue of beam attenuation, i.e. much of the laser energy is absorbed by soot particles and therefore cannot induce signals behind the wall-jet head region. This is evidenced by significantly reduced near-wall signals (either OH-PLIF or PLII). The mismatch between OH* chemiluminescence and OH-PLIF signal distributions is also due to the beam attenuation. However, the soot concentration is very high in the wall-jet head region, and some near-wall soot signals are also observed, indicating higher soot production and wide distributions of soot pockets for regular diesel. Importantly, the soot region of methyl decanoate is less and the concentration is lower, causing the soot pockets to be surrounded by OH radicals. In addition to lower soot formation of oxygenated biodiesel, this soot-OH distribution characteristic promotes the soot oxidation, leading to much lower in-cylinder soot concentration. Indeed, at the latest crank angle location, the remaining soot signal is stronger for regular diesel despite the beam attenuation.

Based on laser-based images of diesel and biodiesel flame and soot distributions, a postulated conceptual model of diesel/biodiesel combustion has been developed as illustrated in Figure 2-5. For both fuels, during the ignition delay period, the injected fuel initially travels as a free jet before impinging on the bowl wall to form a wall-interacting jet. Upon the wall-impingement, the fuel jet

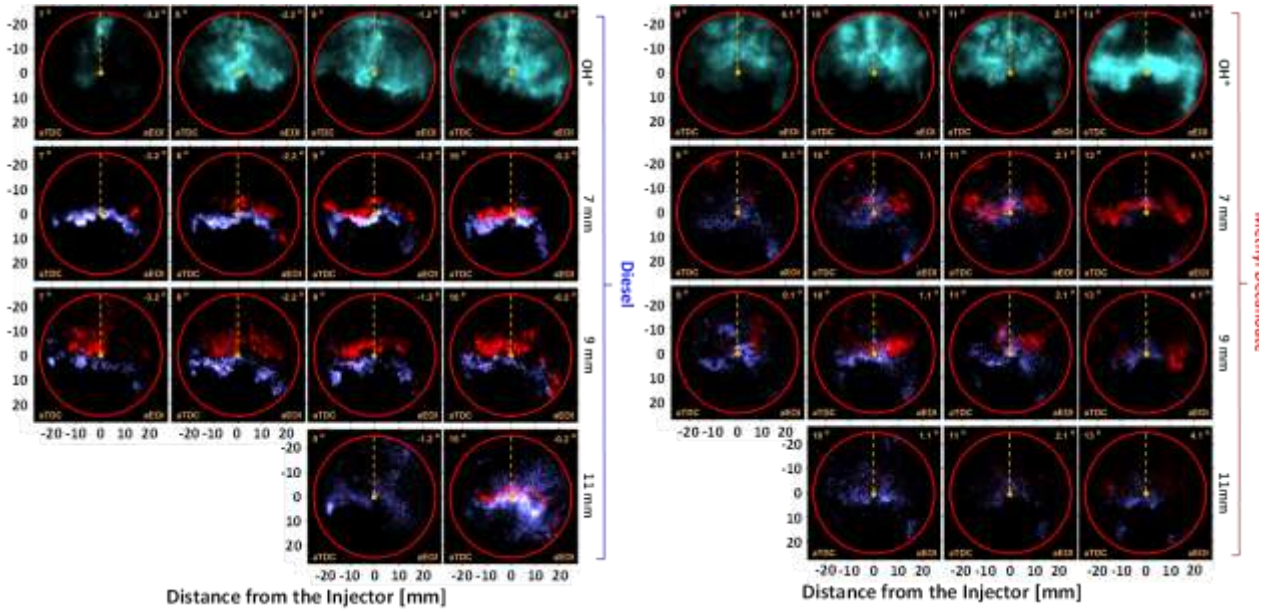

Figure 2-4. OH* chemiluminescence (top) and combined OH-PLIF and PLII images (bottom) for regular diesel (left) and a biodiesel surrogate fuel (right).

flows along the bowl wall while at the same time bounces off the bowl wall and travels back towards the nozzle. The latter movement occurs below the free jet trajectory and along the bottom surface of the bowl. The cool-flame region grows quickly, matching the size of the fuel jet in the head region. Up to this point, both fuels show great similarity.

During the premixed burn phase, however, the transition from the low-temperature reaction to high-temperature reaction occurs much faster for biodiesel. The OH first appears in the leading edge of the penetrating wall-jet, which is followed by the wall-jet head region. The high-temperature reaction expands throughout the wall-jet head region at which the peak rate of the apparent heat release is measured. The OH coverage area grows at a higher rate for biodiesel due to long-stretched carbon chain structure and the presence of O atoms in the fuel. As the injection ends in the middle of the premixed burn phase, the apparent heat release rate declines and the mixing-controlled burn commences. For regular diesel, the soot formation first occurs at the start of mixing-controlled burn and from the fuel-rich region near the wall-impingement point. This occurs at much later timings for biodiesel and the concentration is lower due to less soot formation in the oxygenated fuel. The soot region continues to grow with the increasing number of soot pockets and various sizes and shapes. For regular diesel, the signal is strong throughout the flame region whereas the biodiesel soot is surrounded by OH radicals. For both fuels, the soot pockets shrink in size as the OH radicals are consumed to oxidise soot particles. This OH-induced soot oxidation is much higher for biodiesel as OH radicals trap soot pockets. As a result, the remaining soot signals are stronger for regular diesel, which explains why the engine-out soot emissions are higher.

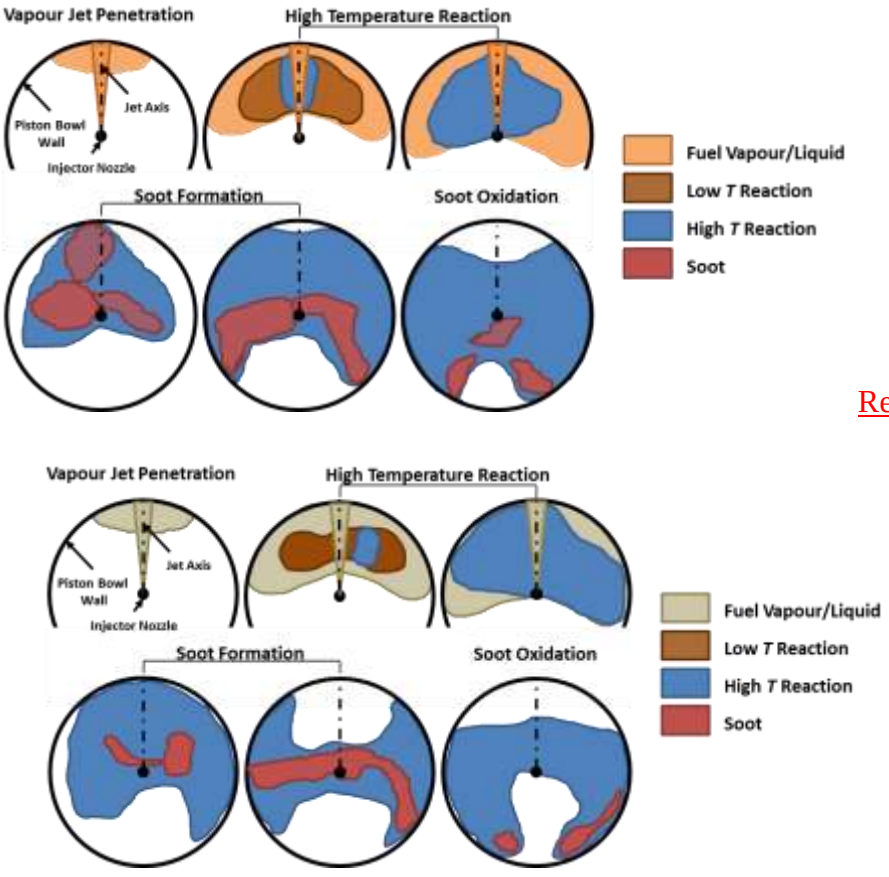

Figure 2-5. Illustration of the development of fuel, low-temperature reaction, high-temperature reaction, and soot of a single fuel jet in a small-bore diesel engine for regular diesel (top) and a biodiesel surrogate fuel (bottom).

Milestone 3: In-flame soot sampling and structure analysis

In the same engine and operating conditions used for laser-based imaging diagnostics of OH and soot, the direct soot sampling experiments from diesel and biodiesel flames has been conducted. This soot sampling work has produced two high-quality journal papers (**Publication 10-11**) and currently two more journal papers are in preparation using the data obtained from this project (unlisted). A brief summary of soot sampling results for both regular diesel and biodiesel fuels is provided in this report.

Figure 3-1 shows natural combustion signals (i.e. hot soot luminosity signals) obtained from the cylinder of our optical diesel engine during this soot sampling experiment. The images on the top and mid rows suggest that sooting flame develops on the fuel jet trajectory (illustrated by orange dashed line directing 2 o'clock) and then penetrates along the piston-bowl wall. Shown at the bottom for images through a cylinder liner window (i.e. side-view images) indicate that the sooting flame breaks into two soot pockets upon the impingement on the bowl wall and then flows along the wall, consistent with the "bottom-view" images above. The horizontal red bar indicates the sampling location, suggesting that thermophoresis-based hot soot particle deposition on a cold TEM grid layer can occur successfully.

Soot particle morphology

The sampled soot particles were imaged using transmission electron microscopes for the analysis of size and structures. Figure 3-2 (left) shows example soot particle images of regular diesel, indicating that the in-flame soot particles are complex aggregates with various fractal-like structures ranging from long-stretched chain structures to compact agglomerates. The differences between regular diesel and biodiesel soot structures are striking. The soot particle images shown in Figure 3-2 (right)

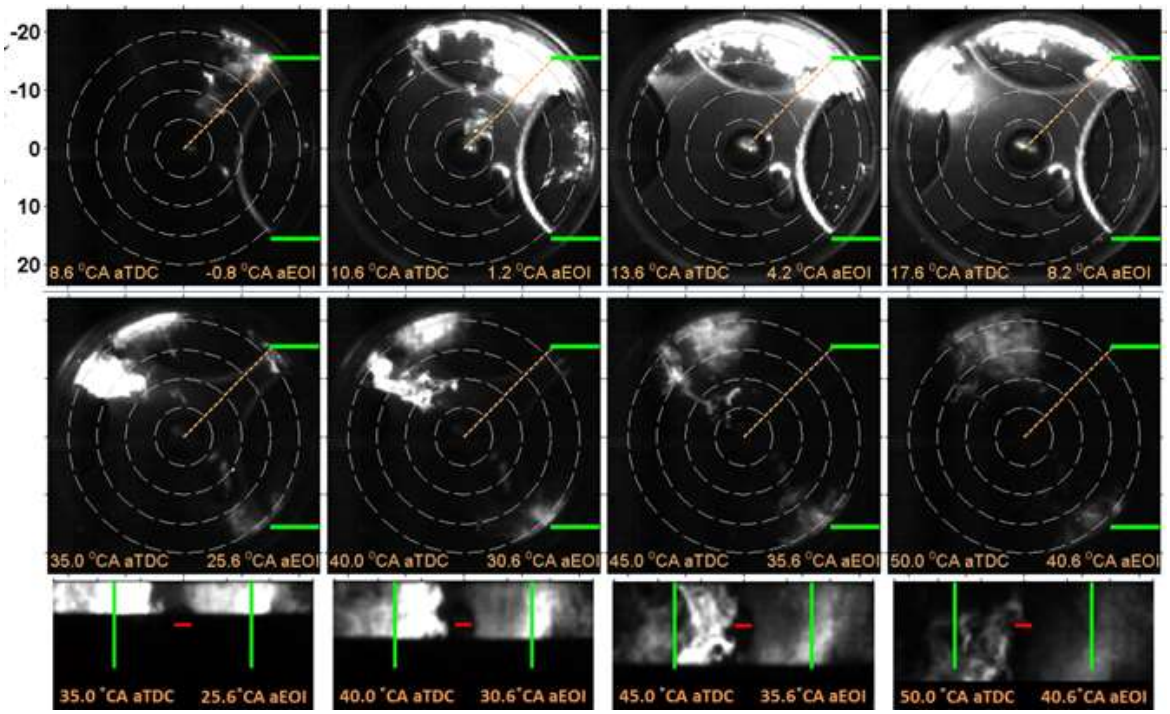

Figure 3-1 Still images from two-camera-based high-speed movies showing hot soot luminosity of regular diesel.

indicate that the size of biodiesel soot particles is much lower than that of regular diesel and has simpler structures. In fact, the soot aggregates of methyl decanoate are so small that many of them are monomer (single-primary aggregate) or dimers (two-primary aggregate). Such small soot particles can easily be oxidized before they exit through the exhaust, which is consistent with the lower soot LII signals for methyl decanoate (see Figure 2-4). The quantitative analysis of particle size was conducted as shown in Figure 3-3 for the probability density function (i.e. likelihood of having certain soot aggregate size). The mean radius of gyration of methyl decanoate is only one third of regular diesel due primarily to very many soot particles in the 10 nm range. By contrast, diesel soot particles are primarily 40 nm in the mean radius or larger with some of them being 100-nm radius particle or larger.

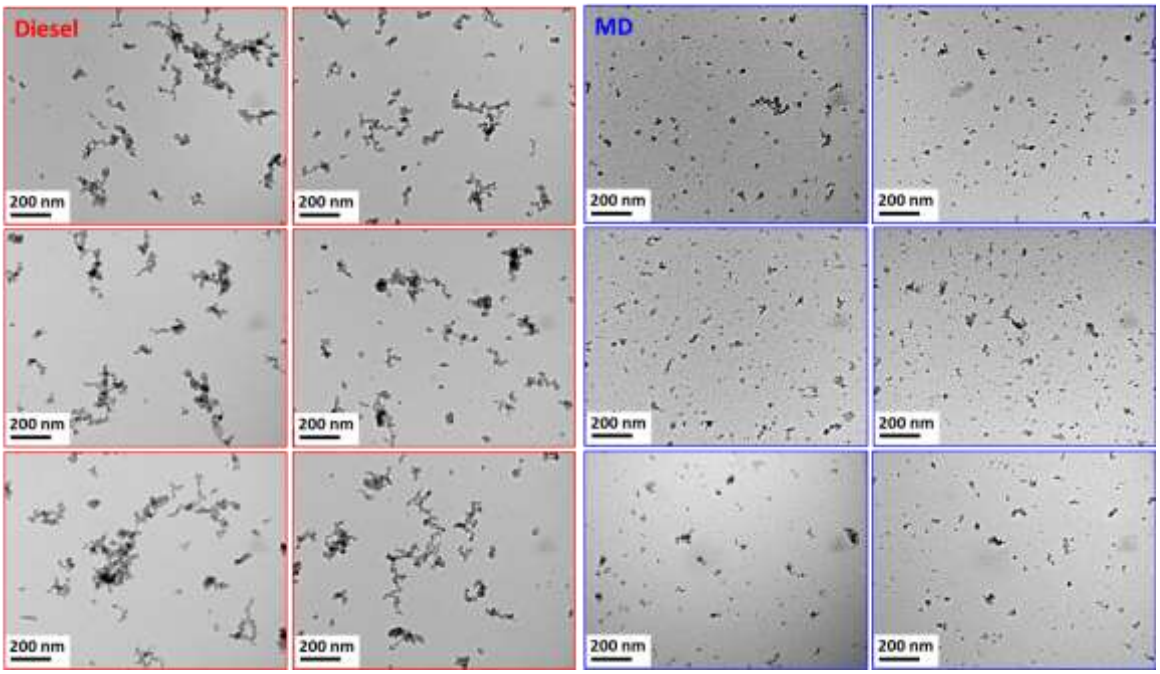

Figure 3-2 Thermophoretically sampled in-flame soot particles of regular diesel (left) and methyl decanoate (right)

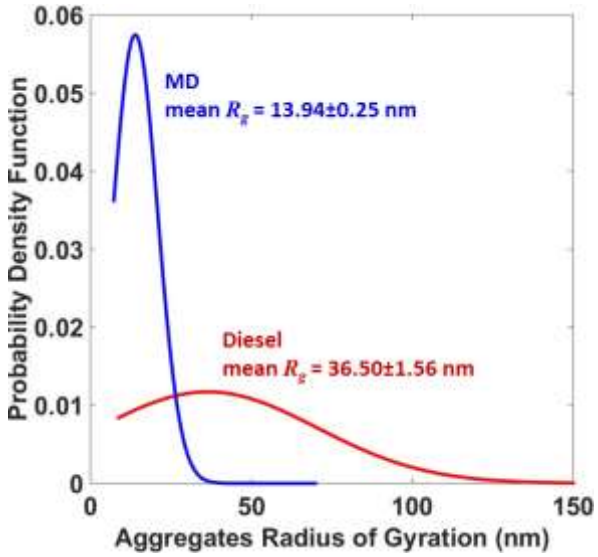

Figure 3-3 The size of soot particles in radius of gyration for regular diesel (red) and methyl decanoate (blue).

Soot particle nanostructure

In addition to soot particle size analysis, the nano-scale carbon fringe analysis has also been performed for both regular diesel and biodiesel fuels. The results are shown in Figure 3-4. For the visualisation of carbon nanostructures, it is necessary to use a lacy TEM grid for the particles sampling so that the extruded portion of the soot particles attached to the breached carbon layers of the TEM grid are used for the flat background imaging. This is illustrated in Figure 3-4. The highly magnified TEM images show that soot particles comprise of many carbon fringes forming multiple core sections surrounded by an outer shell section. The images show that the core fringes are randomly orientated whereas the shell fringes are well aligned. Between diesel and methyl decanoate, the fringe separation distance appears to be lower for the biodiesel surrogate. This means biodiesel soot particles were further oxidized before they were sampled directly from the flame. The higher oxidation status is once again consistent with the laser images (Figure 2-4) showing the soot pockets surrounded by soot-oxidizing OH radicals.

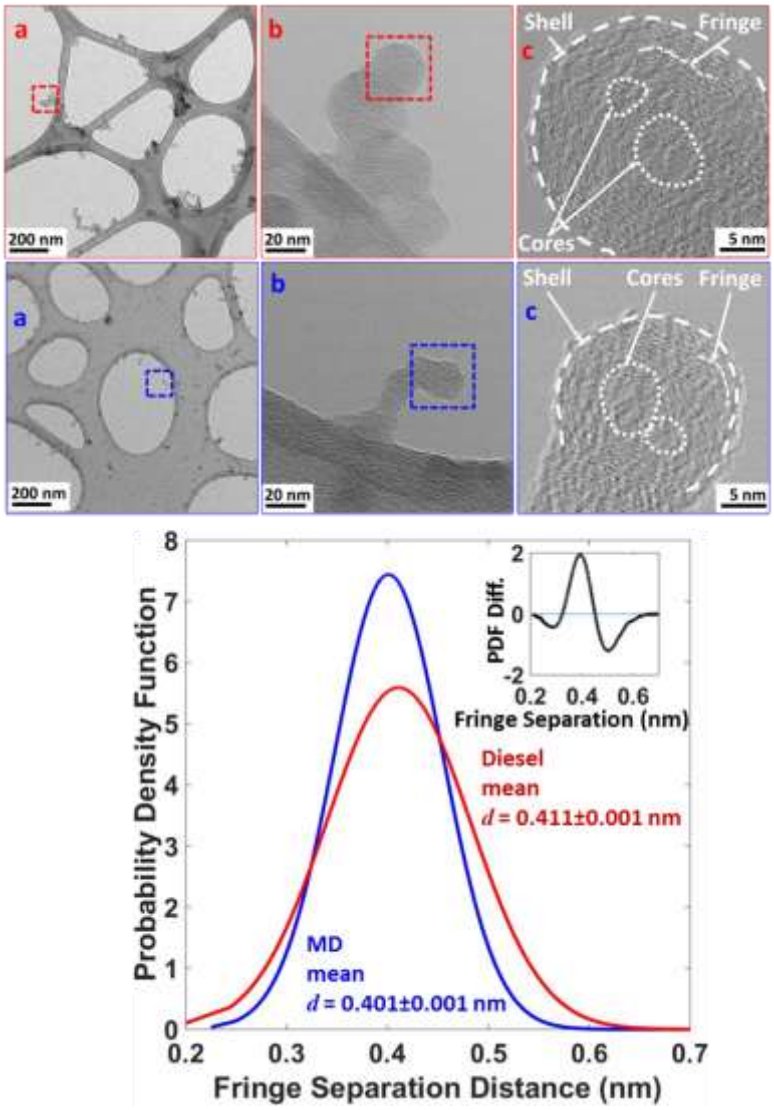

Figure 3-4 Sampled soot particles on lacy TEM grids for nano-scale carbon fringe analysis for regular diesel (top) and methyl decanoate (middle). Shown at the bottom are the probability density function distributions of carbon fringe-to-fringe separation distance based on over 10,000 carbon fringes for each fuel.

Milestone 4: Engine performance emissions testing results

A metal engine sharing the same engine dimension and fuel injection system of the optical diesel was used to conduct performance and emissions testing of diesel and biodiesel blended in diesel. This engine performance and emissions testing has led to three papers (**Publication 12-14**). A brief summary of major findings are presented in this report.

Effects of biodiesel production process

Two 10% biodiesel blends and regular diesel were tested for in-cylinder phenomena and engine-out emissions. The selected biodiesels were 10% methyl-ester biodiesel using a chemical catalyst blended ($B10_{mc}$) and 10% ethyl-ester biodiesel using a biological catalyst ($B10_{eb}$) blended with 90% petroleum diesel. In addition to this fuel variation, the injection timing was also varied.

Figure 4-1 shows that, despite similar in-cylinder pressure and apparent heat release rate traces during the main combustion, the indicated mean effective pressure (IMEP) of B10 fuels are found to be lower than that of diesel due to extended burn duration in the late stage of diesel combustion. Since the faster burning improves the combustion by releasing heat energy in short time and thereby enhancing the subsequent reactions, the long burn duration of B10 fuels causes the decreased IMEP. Therefore, the tested B10 fuels of this study have drawbacks in the indicated power.

By contrast, figure 4-2 shows that the brake mean effective pressure (BMEP) of B10 fuels appear to be higher than that of diesel. It should be noted that the difference between IMEP and BMEP is friction mean effective pressure (FMEP), an important efficiency loss parameter associated with mechanical losses in the joints and fuel pumps as well as a pumping loss. In Figure 4-2, FMEP is very high due to the single cylinder engine operation of this study but the trends is clear for higher FMEP of diesel than that of B10 fuels. Therefore, it is explained that the enhanced lubricity of biodiesel blends caused the decreased frictional loss, which outperformed the IMEP reduction. This advantage is very evident for $B10_{eb}$.

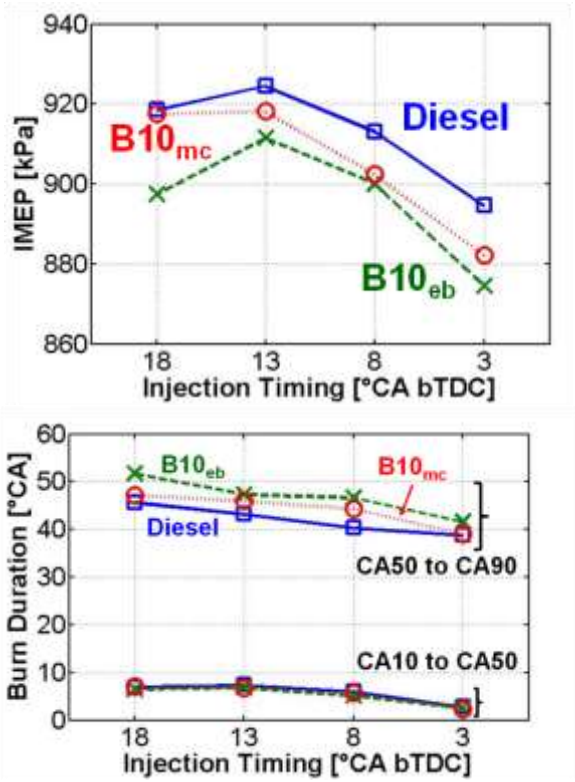

Figure 4-1. Effect of injection timing on IMEP and burn duration for diesel, $B10_{mc}$ and $B10_{eb}$ fuels.

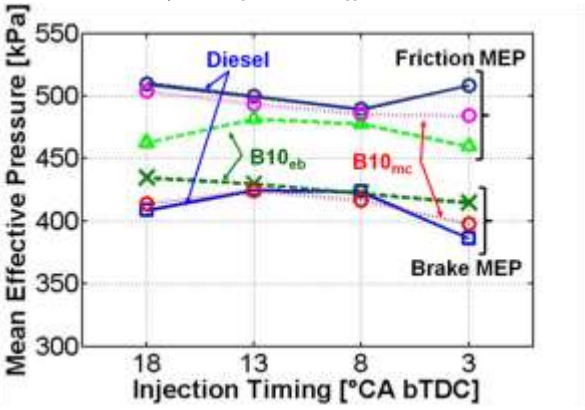

Figure 4-2. Effect of injection timing on BMEP and FMEP for petroleum diesel, $B10_{mc}$ and $B10_{eb}$ fuels.

Engine-out emissions were also measured for the same engine operating conditions. Figure 4-3 shows interesting trends CO/HC such as lower CO emission of B10 fuels than that of diesel due to enhanced oxidation of oxygenated fuels but higher HC emissions due to the wall wetting and fuel trapping in the crevice volume. However, their significance evaluated using the combustion efficiency analysis is very low. The smoke emissions of B10 fuels show marked differences with regular diesel with lower opacity levels for both B10 fuels. In particular, the ethyl ester biodiesel blend ($B10_{eb}$) achieves 62% smoke reduction compared to regular diesel. It is explained that oxygenated biodiesel blends suppress the soot formation while enhancing the oxidation and this effect was higher for ethyl esters compared to methyl esters. For NO_x emissions, different trends are observed for the two biodiesel blends. The $B10_{eb}$ fuel shows reduced NO_x emissions because the flame temperature is reduced due to lower calorific value and shorter carbon chain length of the used triglycerides. However, $B10_{mc}$ fuel exhibits the increased NO_x emissions as the flame temperature increases due likely to short alcohol chain lengths.

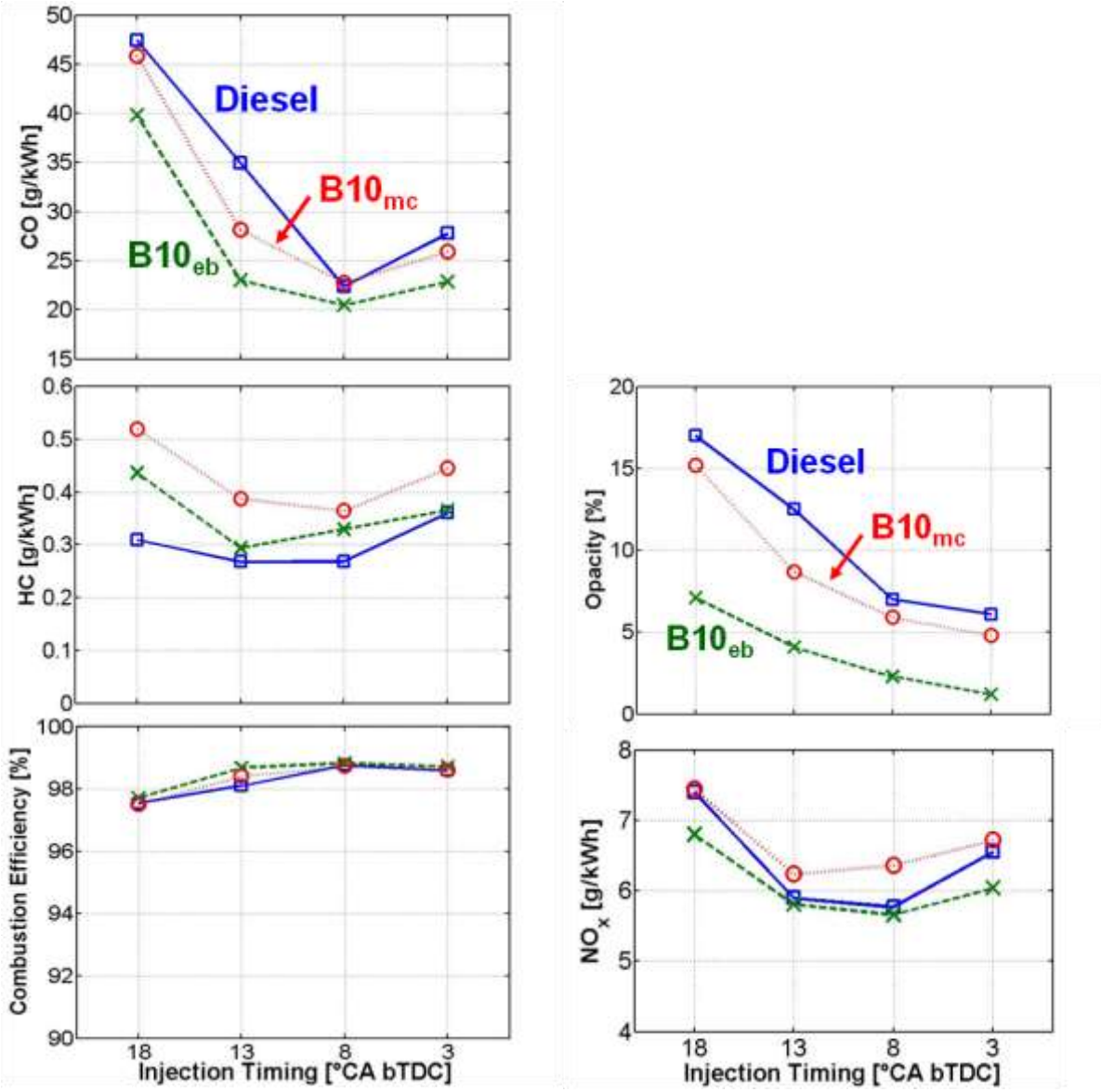

Figure 4-3. Effect of injection timing on CO/HC and combustion efficiency (left) and opacity (smoke) and NOx emissions for diesel, $B10_{mc}$ and $B10_{eb}$ fuels.

Biodiesel blending ratio variations

Various blends of regular diesel and lipase-catalysed oil-based ethyl ester biodiesel were tested for global in-cylinder phenomena and engine-out emissions. The specific goal was to identify the maximum biodiesel blending ratio that can produce comparable brake power of diesel combustion while still taking some advantages of emissions reduction.

Figure 4-4 suggests that for higher biodiesel blends, the lower calorific value of biodiesel and overall leaner mixture cause the decreased diffusion flame temperature and the extended burn duration during the mixing-controlled phase of combustion. As a result, the reaction becomes slower, leading to decreased indicated mean effective pressure. Despite the decreased indicated mean effective pressure of high biodiesel blends, the improved lubricity of biodiesel contributes to reduce friction loses and thereby maintaining similar brake mean effective pressure of regular diesel. However, as shown in Figure 4-5, for fixed total fuel energy conditions of this study, a significant increase in the brake specific fuel consumption (BSFC) is problematic for high biodiesel blends. The advanced fuel injection timing up to 13 CA before TDC can compensate the loss and can achieve up to 40% biodiesel blending ratio to maintain similar fuel conversion efficiency of regular diesel. Higher blending ratio will likely cause unacceptably lower fuel conversion efficiency and BSFC.

The emissions benefits are clearly present for high blending ratio biodiesel fuels as shown in Figure 4-6. Being oxygenated fuel, biodiesel has a high oxidation rate of CO and thereby decreasing engine-out CO emissions. However, the deteriorated atomisation due to high viscosity and the lower fuel volatility are thought to cause the over-penetration of liquid-phase fuel and wall wetting issues, leading to increased unburnt HC emissions. While these interesting trends are observed, the overall combustion efficiency is estimated at over 98% regardless of a biodiesel blending ratio in this study. Therefore, the significance of CO and uHC emission trends is not high.

Due to a well-known effect of oxygenated fuel on suppressed soot formation and enhanced soot oxidation as well as reduced aromatic contents, the engine-out smoke emissions are significantly lower for high biodiesel blends

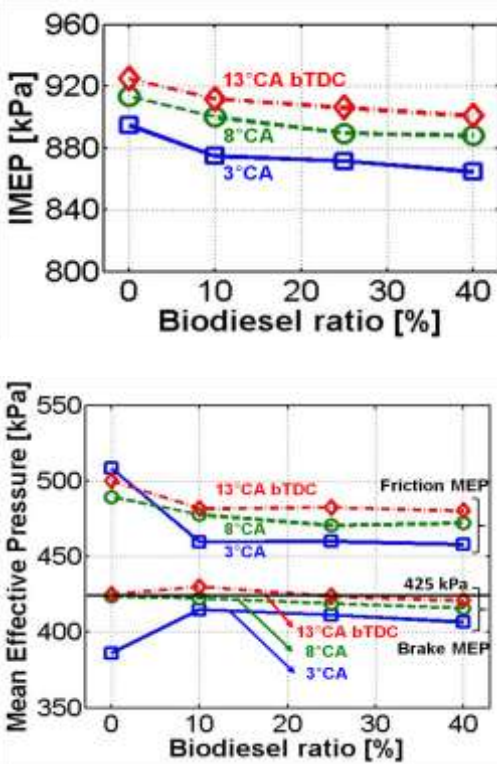

Figure 4-4. Effect of biodiesel blending ratio and fuel injection timing on the mean effective pressures

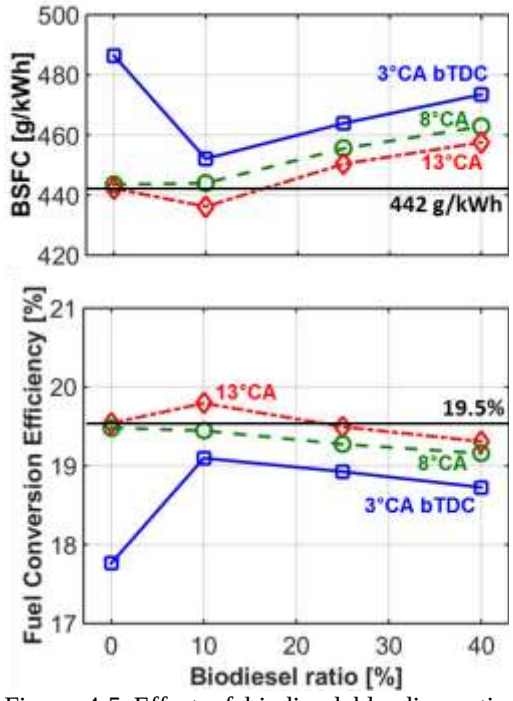

Figure 4-5 Effect of biodiesel blending ratio and fuel injection timing on the brake specific fuel consumption and fuel conversion efficiency

as shown in Figure 4-6. For the tested conditions of this study, over 70% smoke reduction is achieved for B40 compared to petroleum diesel. A great advantage of the tested biodiesel blends is found in decreased NO_x emissions, which can be explained by decreased flame temperature associated with lower calorific value and shorter carbon chain length of the used triglycerides. For B40, over 10% decrease in NO_x emissions is measured compared to petroleum diesel. When the brake specific fuel consumption and smoke/NO_x emissions are considered altogether, however, the maximum biodiesel blending ratio is limited by 40%, suggesting that the full use of reduced emission benefits of high biodiesel blends is not realistic but it has to be compromised for the acceptable brake specific fuel consumption.

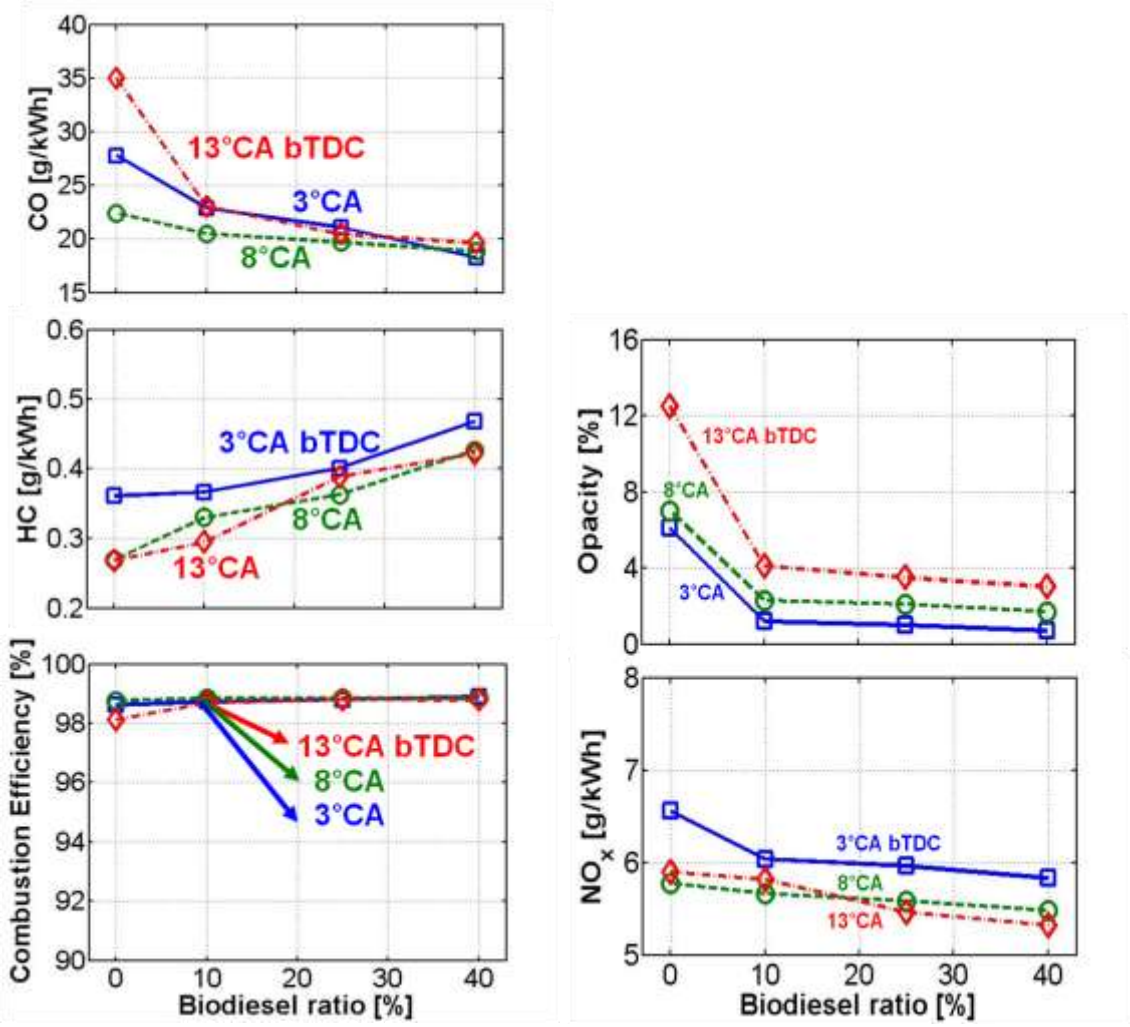

Fig 4-6. Effect of biodiesel blending ratio and fuel injection timing on the emissions of carbon monoxide (CO), unburnt hydrocarbon (HC), opacity (smoke level), and oxides of nitrogen (NO_X). Shown below the HC emissions is the combustion efficiency estimated using the CO and HC emissions.

Concluding Remarks and a Proposal for Follow-up Research

In the current project, using n-dodecane and methyl decanoate as surrogate fuels, detailed modelling based on transport probability density function (TPDF) methods and laser-based imaging diagnostics of high-temperature reaction zones and soot regions in an optical diesel engine has led to enhanced understanding of soot reduction mechanism in biodiesel combustion.

Motivation: It is now necessary to further develop this well-established methodology to address a key question about the effect of biodiesel molecular structures on soot formation and oxidation. Two excellent candidates are the carbon chain length and the unsaturation level, which, from previous engine performance tests, are found to impact the tailpipe emissions significantly. For example, biodiesel fuels with shorter carbon chain length lead to lower soot and NOx emissions; however, a fuel consumption penalty is unavoidable. It has also been shown that higher unsaturation level of biodiesel fuels causes reduced soot but higher NOx emissions. While these trends are known, there are virtually no physical explanations available due to the lack of fundamental data either from advanced diagnostics or numerical simulations.

Approach: We will address this issue by performing laser-based imaging of in-cylinder soot together with another laser-based imaging of hydroxyl radicals in optical combustion facilities including a constant-volume high-pressure vessel and an optically accessible diesel engine. The hydroxyl radicals are a good marker of high-temperature reactions and hence can show the thermal NO formation regions inside the cylinder of the engine. The experiments will be supported by advanced modelling first to demonstrate predictive capability for fuel chemistry effects and second to clarify the underlying physics and chemistry of biodiesel combustion. The engine modelling will consider the full cycle including intake and exhaust geometry, complete with moving valves and piston, while the chamber modelling will focus on advanced closures for turbulence-chemistry interactions. Detailed comparisons between model and experiment will provide valuable guidance for model selection and offer detailed interpretations of the in-cylinder phenomena.

Publications

Milestone 1: Numerical simulation

1. Chishty M.A., Bolla M., Hawkes E.R, Pei Y., and Kook S., "Soot formation modelling for n-dodecane sprays using the transported PDF model," Submitted to Combustion and Flame and currently a second revised manuscript in review, 2016.
2. Bolla M., Chishty M.A., Hawkes E.R, Chan Q.N., and Kook S., "Influence of turbulent fluctuations on radiation heat transfer and soot/NO formation under ECN Spray A conditions," Accepted for publication in Proceedings of the Combustion Institute and currently in press, 2016.
3. Chishty M.A., Bolla M., Hawkes E.R, Pei Y., and Kook S., "Assessing the importance of radiative heat transfer for ECN Spray A using the transported PDF method," SAE International Journal of Fuels and Lubricants 9(1):100-107, 2016.
4. Chishty M.A., Bolla M., Pei Y., Hawkes E.R., Kook S., Lu, T., "Soot formation modelling of spray-A using a transported PDF approach," SAE Technical Paper 2015-01-1849, presented at JSAE/SAE International Powertrains, Fuels and Lubricants Meeting, Kyoto, Japan, Sep, 2015.
5. Chishty M.A., Bolla M., Hawkes E.R., Pei Y., and Kook S., "The effect of radiation heat transfer under ECN Spray A conditions," Australian Combustion Symposium 2015, Paper No. 1E03, Melbourne, Australia, Dec, 2015.

Milestone 2: Laser-based imaging

6. Le M.K., Zhang R., Rao L., Kook S., and Hawkes E.R., "The development of hydroxyl and soot in a methyl decanoate-fuelled automotive-size optical diesel engine," FUEL 166:320-332, 2016.
7. Le M.K. and Kook S., "Injection pressure effects on the flame development in a light-duty optical diesel engine," SAE International Journal of Engines 8(2):609-624, 2015.
8. Le M.K., Kook S., and Hawkes E.R., "The planar imaging of laser induced fluorescence of fuel and hydroxyl for a wall-interacting jet in a single-cylinder, automotive-size, optically accessible diesel engine," FUEL 140:143–155, 2015.
9. Le M.K., Zhang R., Rao L., and Kook S., "Applications of OH-PLIF and soot-PLII in a small-bore optical diesel engine," 7th Australian Conference on Laser Diagnostics in Fluid Mechanics and Combustion, Paper No. P4, Melbourne, Australia, Dec, 2015.

Milestone 3: Soot particle structures

10. Le M.K., Zhang Y., Zhang R., Rao L., Kook S., Chan Q.N., and Hawkes E.R., "Effect of jet-jet interactions on soot formation in a small-bore diesel engine," Accepted for publication in Proceedings of the Combustion Institute and currently in press, 2016.
11. Zhang Y., Zhang R. and Kook S., "Nanostructure analysis of in-flame soot particles under the influence of jet-jet interactions in a light-duty diesel engine," SAE International Journal of Engines, 8(5):2213-2226, 2015.

Milestone 4: Engine performance

12. Woo C., Kook S., Hawkes E.R., Rogers P.L., and Marquis C., "Dependency of engine combustion on blending ratio variations of lipase-catalysed coconut oil biodiesel and petroleum diesel," FUEL 169:146-157, 2016
13. Woo C., Kook S., Hawkes E.R., Rogers P.L., and Marquis C., "A comparative analysis on engine performance of a conventional diesel fuel and 10% biodiesel blends produced from coconut oils," SAE International Journal of Fuels and Lubricants, 8(3):597-609, 2015.
14. Woo C., Kook S., Hawkes E.R., Rogers P.L., and Marquis C., "Engine combustion and emissions of coconut oil-based biodiesel and diesel blends," 19th Australasian Fluid Mechanics Conference, Paper No. 440, Melbourne, Australia, Dec 2014.